# Spatiotemporal scales of motion and particle clustering in free-surface turbulence

Yaxing Li,[1,2,*,†] Henri Sanness Salmon,[1,*] Roumaissa Hassaini,[1] Kelken Chang,[1] Claudio Mucignat,[3] and Filippo Coletti[1]

[1]*Department of Mechanical and Process Engineering, ETH Zürich, Zürich, Switzerland*
[2]*Department of Engineering Mechanics, School of Aeronautics and Astronautics, Zhejiang University, Hangzhou, China*
[3]*Swiss Federal Laboratories for Materials Science and Technology (Empa), Dübendorf, Switzerland*

(Received 6 November 2024; accepted 18 February 2025; published 7 March 2025)

The turbulence below a free surface leaves a footprint on the motion and spatial distribution of floating objects. Here, we investigate the spatial and temporal scales that characterize the transport of small floating particles, resulting from the interplay between the two-dimensional (2D) free-surface dynamics and the three-dimensional (3D) nature of the underlying turbulent flow. We focus on regimes in which the turbulence far below the surface is homogeneous and unsheared, with gravity and interfacial tension maintaining the surface almost flat. Experiments are carried out in two flumes of different sizes, over the fully developed region behind square mesh grids. The subsurface turbulence is characterized by particle image velocimetry over surface-normal and surface-parallel planes, while the motion along the free surface is investigated by tracking millimeter-sized floating spheres and rods. Several single-point statistics of the surface flow reflect the three-dimensional character of the turbulence underneath, e.g., strong intermittency of the particle accelerations. Specific aspects of the surface flow, however, influence the spatial distribution of the floating particles, such as the compressibility of the velocity field and the persistence of surface-attached vortices. The particles cluster over spatial and temporal scales comparable to the integral scales of the turbulence, revealing the critical influence of the subsurface large eddies on the surface dynamics. We propose a mechanism by which particles stick to the long-lived surface-attached vortices swept by the energetic subsurface motions, resulting in the observed large-scale and long-lived clusters.

DOI: 10.1103/PhysRevFluids.10.034602

## I. INTRODUCTION

Turbulent free surface flows are ubiquitous, including virtually all natural bodies of water. The interaction between the turbulence in the bulk and the free surface is crucial to determining the transport properties in terms of mass, momentum, and energy. These play a paramount role at the global scale, e.g., for the enthalpy flux, gas exchange, and aerosol generation at the air-water interface of oceans, rivers, and lakes [1–3], and for the spreading of floating micro- and macroplastics [4,5]. In the presence of large deformations of the surface, the problem is complicated by the mutual transfer of energy between the flow in the bulk and the gravity-capillary waves on the surface [6,7]. Even when waves are weak or absent, the turbulent dynamics are deceptively complex [8]. The present study considers this nonwavy regime, in particular focusing on the fundamental case

*These authors contributed equally to this work.
†Contact author: yaxingli@zju.edu.cn

 

in which the turbulence far from the surface is homogeneous. While the effect of the free surface on the turbulence underneath has been studied extensively, we focus here on how the subsurface turbulence reflects itself on the motion along the surface, which is much less understood.

When the near-surface turbulence is too weak to overcome interfacial tension and gravity, i.e., when both the Weber number We and the Frounde number Fr are much smaller than unity, the surface is negligibly deformed and approximates a flat, free-slip lid. Under these conditions, Hunt and Graham [9] proposed a model based on rapid distortion theory that compared favorably with measurements by Uzkan and Reynolds [10] and Thomas and Hancock [11] in shear-free wall-bounded turbulence. The theory described the inviscid process under the no-penetration boundary condition, which dampens the surface-normal velocity fluctuations within a source layer comparable to the integral scale of the turbulence. Their predictions are in general agreement with later experimental and numerical studies [12–16]. Additionally, the zero-stress boundary determines the properties of a thin viscous layer where the surface-parallel stresses are brought to zero [9,17–19]. The topic was reviewed in detail by Magnaudet [8], who discussed the scaling of both layers and argued that [9] theory is valid also at steady state in the limit of high Reynolds numbers. This was recently confirmed by the experiments of Ruth and Coletti [16], who also highlighted the connection between the interscale energy transfer and upwelling/downwelling motions which carry fluid to/from the surface [14,17].

Less is known about the flow along the free surface above the turbulent bulk and the dynamics of floating particles. Previous studies have shown that the free-surface flow features some characteristics of both two-dimensional (2D) and three-dimensional (3D) turbulence. Perot and Moin [17] already conjectured that the reduced dissipation they observed at the surface followed from the two-dimensionality of the flow altering the energy cascade. Several successive works on open channel flows found evidence that the motion along the free surface mimics 2D turbulence, with evidence of an inverse cascade from smaller to larger scales [20], and the prevalence of long-lived vortices [21,22]. Other studies, on the other hand, stressed how the flow remains fully 3D in nature: The free-surface boundary condition does not impede vortex stretching [13,18,23] which is among the main drivers of interscale energy fluxes [24,25]. In a recent field study, Sanness Salmon *et al.* [26] investigated the transport on a meandering stream using floating particles. They found that several fundamental aspects of the surface flow displayed hallmark features of 3D turbulence, including the intermittency of acceleration and rotation rates.

One of the specific features of free-surface flow is the compressible nature of the 2D velocity field, which influences the relative motion of floating particles. Csanady [27], describing results from a field study in Lake Huron, observed that the dispersion of floaters could be completely reverted in the presence of regions of confluence. Later, numerical studies by Eckhardt and Schumacher [28] and Boffetta *et al.* [29] analyzed the nosolenoidal flow along the surface above forced homogeneous turbulence, finding strong intermittency of the velocity differences and intense clustering of floating particles. Goldburg *et al.* [30] and Cressman *et al.* [31] qualitatively confirmed those findings with experiments in their apparatus generating zero-mean flow turbulence. Quantitative comparisons were made difficult by practical challenges in imaging the surface; in particular, due to the agglomeration of highly concentrated submillimeter floating particles [32–34]. These studies were limited to a relatively small Reynolds number ($\mathrm{Re}_\lambda \sim <140$ based on the Taylor microscale $\lambda$ in the bulk) for which the turbulence did not achieve sufficient scale separations for two-point statistics to exhibit power-law scaling [35]. Recently, Li *et al.* [36] considered the relative velocity and dispersion of highly dilute submillimeter floating particles in a large homogeneous turbulence apparatus, achieving $\mathrm{Re}_\lambda = 550$ below the quasi-flat free surface. They found that the effective compressibility of the surface flow leads to anomalously large relative velocities at small separations, which in turn extend the ballistic regime of pair dispersion well into the inertial range of temporal delays.

The above indicates how our understanding of the connection between the dynamics along the 2D surface and the subsurface turbulence still remains incomplete, even in the fundamental and seemingly simple case of small interfacial deformations and homogeneous turbulence far from

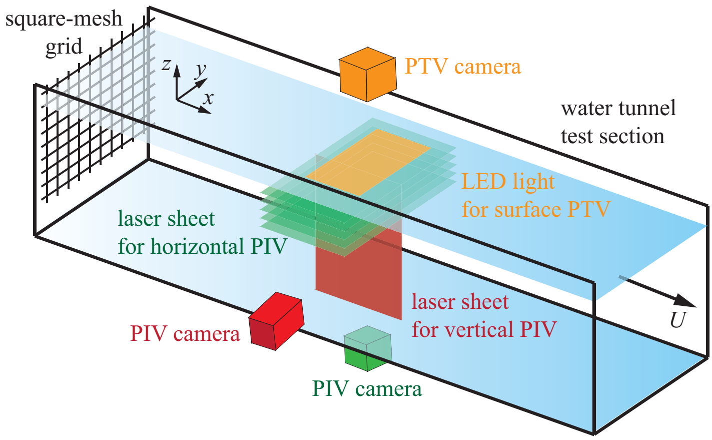


FIG. 1. Schematics of the experimental setup in water tunnels. Three optical diagnostics were carried out to implement PTV on the free surface, 2D PIV on the horizontal plane, and 2D PIV on the vertical plane, respectively.

the open boundary. In this article, which follows from an invited lecture by the last author at the 26th International Congress of Theoretical & Applied Mechanics (Daegu, South Korea), we tackle the following fundamental questions: How does the turbulence underneath imprint its features on the surface? How do the spatial and temporal scales of free-surface flow shape the scales of the clustering of floating particles? To this end, we present laboratory experiments in two water tunnels, where turbulence is generated by a grid. Using particle image velocimetry (PIV) and particle tracking velocimetry (PTV), we characterize the subsurface turbulence as well as the behavior of small floating spheres and rods that follow the flow along the quasi-flat free surface. The paper is organized as follows: In Sec. II, we present the experimental setups (Sec. II A) and the measurement approach (Sec. II B). In Sec. III, we characterize the subsurface turbulence (Sec. III A), the motion along the surface (Sec. III B), and the spatial distribution of the floating particles (Sec. III C). We discuss the results and draw conclusions in Sec. IV.

## II. EXPERIMENTAL METHODS

### A. Laboratory setups

Measurements are carried out in two similar setups of different scales, one located at ETH Zürich and one at the Swiss Federal Laboratories for Materials Science and Technology (Empa). Both of them are recirculating flumes in which a square-mesh, square-bars grid is placed downstream of the contraction that connects to the straight test section, providing a different Reynolds number $\mathrm{Re}_M = U_s M/\nu$ (where $U_s$ is the mean surface velocity, $M$ is the grid spacing, and $\nu$ is the kinematic viscosity). Both facilities were recently described elsewhere [37,38] and only the basic characteristics are given here. A schematic illustrating the flow configuration and imaging systems is depicted in Fig. 1.

The ETH tunnel has a 2 m long, 0.45 m wide test section, whereas the Empa tunnel has a 6 m long, 1 m wide test section. The main flow parameters are summarized in Table I. In both setups, the grids have a solidity of 0.31 and the free surface is about $0.8M$ above the topmost immersed horizontal bar. In the following, we will refer to the measurements in ETH and Empa tunnels as the cases $\mathrm{Re}_M = 8350$ and $\mathrm{Re}_M = 24\,000$, respectively. The streamwise (surface-parallel), spanwise, and vertical (surface-normal) upward directions are indicated by $x$, $y$, and $z$, respectively, with origin at the grid location ($x = 0$), on the channel centreline ($y = 0$) and at the water surface ($z = 0$). The velocities in $x$, $y$, and $z$ are denoted as $U$, $V$, and $W$, respectively. Fluctuations are obtained by

TABLE I. Main parameters characterizing the flow in the two utilized flumes. $U_s$ is the mean free-surface velocity, $M$ is the mesh grid spacing, and $H$ is the water depth. $u_{\mathrm{rms}}$ is the streamwise rms velocity, $w_{\mathrm{rms}}$ is the vertical rms velocity, $L$ is the integral length scale, $\epsilon$ is the dissipation rate, $\eta$ is the Kolmogorov length scale, and $\tau_\eta$ is the Kolmogorov time scale. The turbulence properties are evaluated in the bulk (i.e., more than one integral scale below the surface).

| | $U_s$ [m/s] | $M$ [mm] | $H$ [m] | $u_{\mathrm{rms}}$ [mm/s] | $w_{\mathrm{rms}}$ [mm/s] | $L$ [mm] | $\epsilon$ [mm$^2$/s$^3$] | $\eta$ [mm] | $\tau_\eta$ [s] | $\mathrm{Re}_M$ | $\mathrm{Re}_\lambda$ | Fr | We |
|---|---|---|---|---|---|---|---|---|---|---|---|---|---|
| ETH tunnel | 0.24 | 35 | 0.4 | 6.7 | 6.4 | 14.2 | 21.6 | 0.46 | 0.22 | 8350 | 38 | 0.12 | 0.01 |
| Empa tunnel | 0.30 | 80 | 0.4 | 16.5 | 15.6 | 96 | 39.1 | 0.40 | 0.16 | 24000 | 169 | 0.15 | 0.37 |

Reynolds decomposition: $U = \langle U \rangle + u$, $V = \langle V \rangle + v$, and $W = \langle W \rangle + w$, where angle brackets denote ensemble/temporal averaging. Table I also reports the main turbulence properties in the bulk (i.e., more than one integral scale below the surface), measured by PIV as described below. These include the root mean square (rms) fluctuations in the streamwise ($u_{\mathrm{rms}}$) and vertical ($w_{\mathrm{rms}}$) directions, the longitudinal integral scale $L$, the dissipation rate $\epsilon$, the Kolmogorov length scale $\eta = (\nu^3/\epsilon)^{1/4}$ and time scale $\tau_\eta = (\nu/\epsilon)^{1/2}$, and the Taylor Reynolds number $\mathrm{Re}_\lambda = \lambda u_{\mathrm{rms}}/\nu$, where $\lambda = \sqrt{15}\tau_\eta u_{\mathrm{rms}}$ is the Taylor microscale.

Although the presence of the grid perturbs the water surface locally, the waves mostly dissipate within $\mathcal{O}(10M)$ from it, well upstream of the measurement location. Indeed, consistent with the small values of the Froude number $\mathrm{Fr} = U_s/\sqrt{gH}$ (where $H$ is the water depth), the surface deformation is minimal: Within the measurement field of view (FOV), the wave amplitude is smaller than 0.5 mm, as estimated from photographs taken through the transparent sidewalls of the test sections. This is similar to the conditions in the grid-stirred tank of [30,31], where surface waves contributed negligibly to the motions of floating particles. The water surface is skimmed with a fine fishnet before every experiment to minimize the accumulation of surfactants. The surface tension is measured via a Du Noüy ring at various time points during the experimental campaigns, yielding no significant variations around the standard value of 0.07 N/m. The Weber number $We = \rho u_{\mathrm{rms}}^2 L/\sigma < 1$ confirms that surface tension contributes to maintaining the surface quasi-flat.

### B. Measurement approach

The subsurface turbulence is characterized by the PIV of microscopic tracers (hollow glass spheres, 10 μm and 1.1 g/cm$^3$), while the surface motion is studied by PTV of millimetric floating particles, with the main measurement parameters listed in Table II. The FOVs are located sufficiently far from the grid for the turbulence to reach a fully developed state in which classic scaling relations apply [39,40]. Measurements along and below the surface indicate that both the mean flow and the turbulence properties have a high degree of homogeneity (within less than 10% of the spatial average) in the spanwise direction.

TABLE II. Imaging parameters for the PIV and PTV measurements in the two considered cases.

| | Focal Length | FOV | Resolution | Acquisition frequency | Measurement range [$x/M$] |
|---|---|---|---|---|---|
| PIV $\mathrm{Re}_M = 24\,000$ | 100 mm | 0.06 m × 0.06 m | 33.6 pixel/mm | 1 Hz | 38.0–38.8 |
| PIV $\mathrm{Re}_M = 8350$ | 100 mm | 0.08 m × 0.05 m | 32.0 pixel/mm | 1 Hz | 28.7–31.0 |
| PTV $\mathrm{Re}_M = 24\,000$ | 35 mm | 0.5 m × 0.5 m | 4.4 pixel/mm | 90 Hz | 38.0–44.0 |
| PTV $\mathrm{Re}_M = 8350$ | 35 mm | 0.35 m × 0.5 m | 8.4 pixel/mm | 80–90 Hz | 23.0–37.0 |

In both setups, PIV is performed over streamwise vertical planes at the mid-span of the test section ($y = 0$), using a double-pulsed Nd-YAG laser shone through the transparent tunnel floor and synchronized to a digital camera (4 megapixel Veo 640 CMOS for $\mathrm{Re}_M = 8350$; and 5.5 megapixel CCD Dantec Dynamics for $\mathrm{Re}_M = 24\,000$). For the case $\mathrm{Re}_M = 8350$, three vertically stacked FOVs are stitched together to cover a depth of 120 mm from the surface. Moreover, PIV is performed along five horizontal planes at various depths, shining the laser through the transparent side wall and imaging through the floor. Diffraction and reflection at the air-water interface prevent accurate measurements less than $\sim$1 mm from the surface. Two steps of interrogation window refinement result in a spatial resolution of $\sim 2\eta$, which allows us to capture the fine scale of the turbulence and to calculate spatial derivatives via a second-order central difference scheme. This is applied on the vector field obtained with 50% overlap, after a Gaussian filter of the size of the interrogation window [41]. Statistics are calculated by averaging over 6000 instantaneous uncorrelated realizations.

The dissipation rate $\epsilon$ is obtained by differentiation of the velocity field and using the axisymmetric turbulence approximation of George and Hussein [42]. At the present level of anisotropy, other approaches for the calculation of the missing components of the velocity gradient return marginally different values of $\epsilon$ (e.g., the isotropic assumption yields $\epsilon = 19.5$ mm$^2$/s$^3$). The longitudinal integral scale $L$ is obtained from the exponential fit of the decaying autocorrelation of the velocity fluctuations. We verify that the dissipation rate is consistent with the classic scaling $\epsilon \sim u_{\mathrm{rms}}^3/L$ within a prefactor of order unity [43,44]. At $\mathrm{Re}_M = 24\,000$, where a limited but finite inertial range exists, the dissipation can also be estimated from the second-order velocity structure function [45] and is found to agree within about 10% with the velocity-gradient-based measurement.

For the PTV measurement of the surface velocity, size-selected polyethylene spheres (Cospheric LLC, specific gravity $\sim$0.95) are dispersed in the flow downstream of the grids by manually shaking a custom-made vial rack. Two sphere diameters are considered: 1 mm and 2 mm. When dispensing the spheres, care is taken in keeping low concentrations, $c = \mathcal{O}(10^3)$ m$^{-2}$. This yields typical interparticle gaps much larger than their diameter, such that their hydrodynamic interactions are negligible [34]. Assuming that the dissipation rate along the surface is similar to the one in the bulk (as verified below), the size of the floating particles can be compared to the Kolmogorov scale. In the case at $\mathrm{Re}_M = 24\,000$, the 1 mm and 2 mm particles are $\sim 2.5\eta$ and $\sim 6\eta$ in size, respectively. In the case at $\mathrm{Re}_M = 8350$, they are $\sim 2\eta$ and $\sim 4\eta$, respectively. Interface-resolved simulations by [46], experiments by [47], and analysis by [48] show that neutrally buoyant particles of diameter up to $\sim 5\eta$ closely approximate fluid tracers. Therefore, we expect the present spherical particles to filter only a marginally small fraction of the turbulent fluctuations. This is confirmed by the fact that the statistics of both particle types are effectively indistinguishable (see Appendix A). We expect therefore that the particles, while not perfect tracers due to their finite size, move in ways that are statistically equivalent to (or negligibly different from) the surface flow. The particles being confined to the surface does not limit their ability to follow the local fluid velocity, as the latter has zero vertical components in the limit of a flat surface. Importantly, the mm-sized particles can be detected over relatively large FOVs, allowing us to characterize the large-scale turbulence dynamics. The particles are recaptured by a nylon net at the outlet of the test section. Approximately 90 000 and 22 000 trajectories for the cases at $\mathrm{Re}_M = 24\,000$ and $\mathrm{Re}_M = 8350$ are reconstructed, respectively, allowing for the convergence of the statistics within a few percent.

The floating particles are illuminated by LED lamps and imaged by a CMOS camera (Baumer, 12 megapixels) suspended above the test section. A de-warping mapping procedure is applied using calibration images of a checkerboard plate [49]. Matte black panels are placed below the transparent floor to increase the contrast of the particle images. These range between four and five pixels, whose centroid is identified after subtracting the minimum-intensity background from each set of images. Particles closer than two diameters from each other are discarded in post-processing. The trajectories are reconstructed via a nearest-neighbor PTV algorithm implemented in an in-house code [50]. Particle velocities and accelerations are determined by convolving the trajectories with the first and second derivatives of a Gaussian kernel, respectively. The duration of the kernel is chosen as 20 and 35 frames for the case at $\mathrm{Re}_M = 24\,000$ and $\mathrm{Re}_M = 8350$, respectively, comparable to the smallest

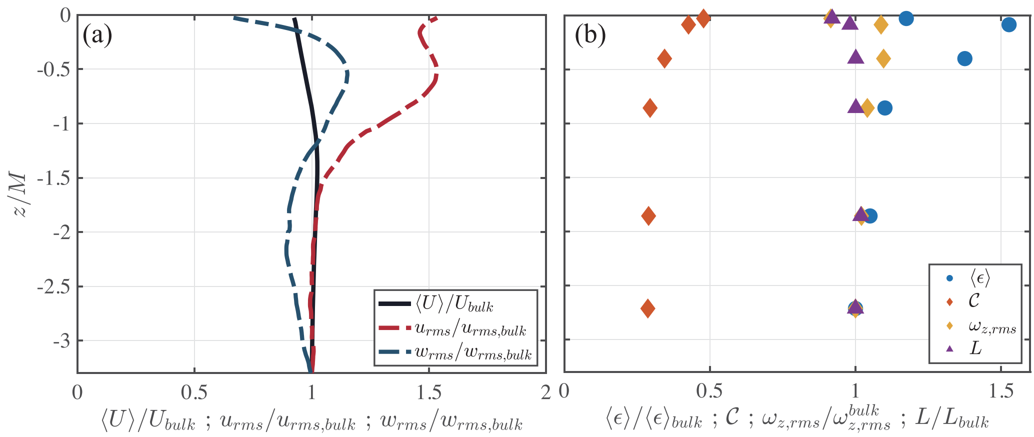


FIG. 2. Surface-normal profiles of (a) mean velocity and rms velocity fluctuations and (b) dissipation rate, compressibility ratio, surface-normal vorticity and integral length scale of the subsurface turbulence, measured by PIV at $\mathrm{Re}_M = 8350$.

time scales of the surface flow. The choice is based on the procedure established by Voth *et al.* [51] and applied in several studies by our group (e.g., Berk and Coletti [52] and Baker and Coletti [53,54]) as well as others (e.g., Gerashchenko *et al.* [55] and Ebrahimian, Sanders, and Ghaemi [56]). In order to probe the rotational dynamics of the free surface, small floating rods are tracked on the surface of the $\mathrm{Re}_M = 8350$ case. These are 2 mm long and 0.35 mm thick and cut out of polypropylene filament (Ebnat AG, specific gravity ∼0.9). Their position, orientation, trajectory, and rotation rate are obtained via a procedure extensively described in Baker and Coletti [54] and Sanness Salmon *et al.* [26]. Briefly, this uses an ellipse fit to the rod image, obtaining the rotation rate by convolution with the first derivative of a Gaussian kernel having the same width as for the spherical particles. Their rotational dynamics are used to investigate the vorticity of the surface velocity field. Elongated particles exhibit rotation rates that may differ from the one of the local fluid due to their tendency to align with the local velocity gradient [57,58]. However, the rotation rate of rods with length within the dissipative range is only moderately attenuated by this effect [59]. Indeed, their rotation can be used to estimate the transverse velocity structure functions and dissipation rate in 3D turbulence [60]. This stand will be confirmed in the following.

## III. RESULTS

In the following, we present selected results from the campaigns conducted at $\mathrm{Re}_M = 8350$ and $\mathrm{Re}_M = 24\,000$. The flow characterization of the case $\mathrm{Re}_M = 8350$ is more extensive, therefore this is used to illustrate the properties of the turbulence below the surface (Sec. III A) and the motion along the surface (Sec. III B). The analysis we present of the spatial distribution and clustering of the particles on the surface (Sec. III C) is based on the case $\mathrm{Re}_M = 24\,000$, for which a larger amount of data on the floating spheres is gathered. We stress that both cases show quantitatively analogous results (as shown in Appendix B). This confirms that the present findings apply at least to the considered range of Reynolds and Froude numbers, and in general support the generality of the conclusions.

### A. Subsurface turbulence

Here, we present key features of the sub-surface turbulence, as measured by PIV along the surface-normal vertical plane. Figure 2(a) shows profiles of the mean and rms fluctuations of the streamwise and vertical velocity, as a function of the depth $z$. While the mean components are largely homogeneous as expected, the fluctuations vary significantly within the source layer of thickness $\mathcal{O}(L)$ [8,9]. The vertical fluctuations monotonically decrease approaching the surface because of the kinematic (no-penetration) boundary condition. On the other hand, the horizontal fluctuations tend to increase due to intercomponent energy redistribution [9]. This behavior is consistent with experiments by Brumley and Jirka [12], Variano and Cowen [15], and Ruth and Coletti [16], as well as simulations by Guo and Shen [14] and Herlina and Wissink [61], among others.

Figure 2(b) presents profiles of higher-order quantities, using data from the surface-parallel PIV planes: the turbulent dissipation rate, the surface-normal vorticity $\omega_{z,rms}$, the integral scale $L$, and the compressibility ratio $\mathcal{C}$. The latter is defined as [29]

$$\mathcal{C} = \frac{\langle(\partial_x u + \partial_y v)^2\rangle}{\langle(\partial_x u)^2\rangle + \langle(\partial_x v)^2\rangle + \langle(\partial_y u)^2\rangle + \langle(\partial_y v)^2\rangle}. \tag{1}$$

The surface-normal vorticity is found to be roughly constant in the vertical direction. This is in agreement with the simulations by Walker, Leighton, and Garza-Rios [13], who found that vortex stretching is balanced by the turbulent transport of enstrophy away from the surface. The dissipation rate first increases within the source layer and then sharply decreases in the viscous layer. This has thickness $L_\nu \sim \sqrt{L\nu/u_{\rm rms}}$ [12,62], which here is $\mathcal{O}(1\text{ mm})$. This behavior, in particular the reduction of dissipation at the surface due to the zero-stress condition, is in line with previous theoretical and numerical studies [14,19].

The compressibility ratio displays a trend similar to what was reported by the simulations by Boffetta *et al.* [29]. These authors found that, in the bulk, $\mathcal{C}$ is comparable to the value of 1/6 expected for a 2D cut of a 3D homogeneous isotropic flow, while close to the surface it approaches 0.5. The integral scale based on the streamwise velocity fluctuations remains approximately constant approaching the free surface. This is at odds with Hunt and Graham's [9] theory, which predicts it to decrease proportionally to the increase of $u_{\rm rms}$. Recent measurements from Ruth and Coletti [16] in a jet-stirred tank show in fact an increase of the surface-parallel integral scale approaching the surface, which they attributed to a hindering of the direct cascade of turbulent kinetic energy (TKE) not captured by rapid distortion theory. The difference with respect to the present case is likely rooted to the different configurations (steady forcing by randomly actuated jets versus decaying grid turbulence) affecting the nonuniversal large scales.

### B. Free-surface turbulence

We first characterize the single-point statistics of the free-surface motion. The probability density functions (PDFs) of both components of the velocity fluctuations and accelerations of the floating particles are presented in Figs. 3(a) and 3(b), respectively. While the velocity fluctuations are close to Gaussian, the accelerations display long, nearly exponential tails. This is a typical feature of 3D turbulence, where the spatial and temporal derivatives of the velocities are strongly intermittent, which is not the case in 2D turbulence [63]. At $\mathrm{Re}_M = 8350$ and 24 000 the kurtosis of the acceleration PDF is ~6 and 12, respectively.

In Fig. 3(c), we report the PDF of the rod rotation rate $\Omega = \dot{\theta}$, where $\theta$ is the rod's orientation angle with respect to the reference $x$ direction. This is strongly intermittent, with a kurtosis of 8.9. The distribution is quantitatively similar to that of $\omega_z$ measured by PIV along the uppermost horizontal plane and shown in the same figure. The rms rotation rate, $\Omega_{\rm rms} = 1.23\,\text{rad/s}$, also agrees closely with $\omega_{z,\rm rms}/2 = 1.12\,\text{rad/s}$ along the same plane. As the latter is at the level of the viscous layer, we expect the surface-normal vorticity herein to reflect the one along the surface. This agreement corroborates the assumption that the rotation rate of the small rods is an appropriate proxy of the fluid rotation, $\Omega \sim \omega_z/2$ [59,60].

In Fig. 4, we display the spatial evolution of the turbulent kinetic energy along the free surface measured from the motion of the spherical particles, $\frac{\langle q^2\rangle}{2} = \frac{\langle u^2\rangle}{2} + \frac{\langle v^2\rangle}{2}$. Applying Taylor's

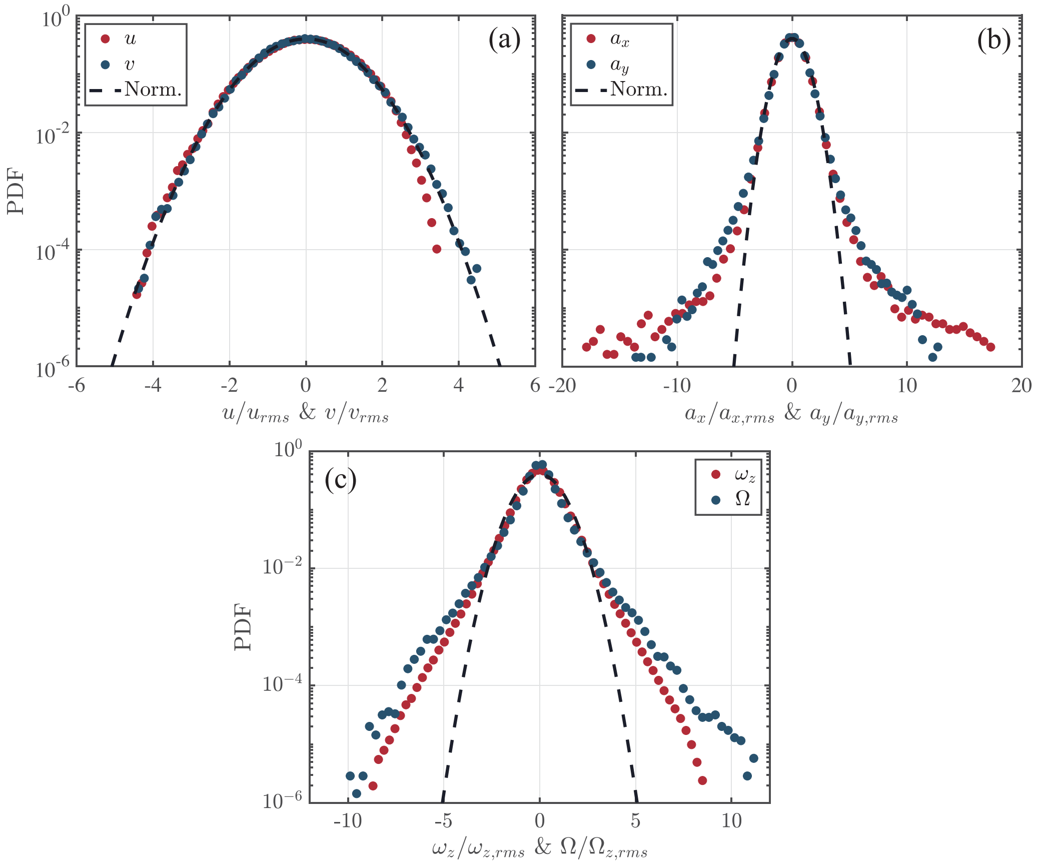


FIG. 3. PDF of the surface-parallel components of (a) velocity fluctuations, (b) accelerations, and (c) surface-normal vorticity and rotation rate measured along the free surface measured by PTV at $\mathrm{Re}_M = 8350$. Dashed lines indicate normal distributions.

hypothesis, we expect

$$\langle q^2 \rangle = A\left(\frac{x}{M} - \frac{x_0}{M}\right)^n, \tag{2}$$

with a decay exponent $-1 > n > -1.4$ (e.g., Lavoie, Djenidi, and Antonia; Hearst and Lavoie; Sinhuber, Bodenschatz, and Bewley [39,64,65]). The latter, along with the constant of proportionality $A$ and the virtual origin $x_0$, is determined by a least-square fit method [39]. The spatial decay of the free-surface turbulent kinetic energy is shown in Fig. 5, which returns $n = -1.23$, consistent with previous studies. The classic relation based on Taylor hypothesis to estimate the dissipation, $\epsilon = -\frac{U}{2}\frac{\mathrm{d}\langle q^2 \rangle}{\mathrm{d}x}$, yields $\epsilon = 2 \times 10^{-5}$ to $9 \times 10^{-6}$ m$^2$/s$^3$ in the measurement range $x/M = 25$–34. This neglects spatial energy fluxes, which are necessarily nonzero as indicated by the vertical profiles in Fig. 2(a). The estimates, however, are comparable to the level of dissipation measured in the bulk, suggesting that the spatial fluxes may be subdominant.

Evaluating $\epsilon$ also allows us to calculate the normalized acceleration variance, $a_0 = \langle a_i'^2 \rangle / (\epsilon^{3/2} \nu^{-1/2})$. In 3D turbulence, we expect $a_0 = \mathcal{O}(1)$ according to the Heiseinberg-Yaglom scaling [51,66]. Sawford *et al.* [67] collected extensive experimental and numerical data and found these could be fit by $a_0 = 5/(1 + 110/Re_\lambda)$, which yields $a_0 = 1.3$ and 3.3 at $\mathrm{Re}_M = 8350$ and 24 000, respectively. These are in close agreement with the acceleration measurements which return $a_0 = 1.2$ and 3.2, respectively.

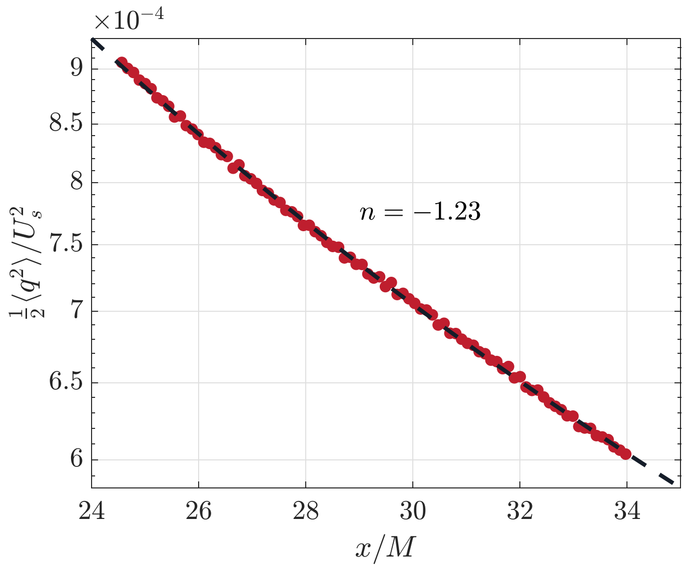


FIG. 4. Normalized TKE of the free-surface flow, measured by PTV at $\mathrm{Re}_M = 8350$, showing the exponential fit based on (2).

In order to characterize the length scales of the turbulent motion along the surface, we calculate the Eulerian autocorrelation of the spheres' velocity fluctuations and rods' rotation rate, $\rho_u^E(r)$ and $\rho_\Omega^E(r)$, respectively, as a function of the separation $r$ Fig. 5(a). While the size of the particles prevents us from probing millimetric separations, the plots give clear indications on the correlation scales. In particular, the velocity fluctuations have characteristic lengths (estimated based on the e-fold decay of $\rho_u^E$) of 14 mm, very close to the integral scale $L$ of the subsurface turbulence. Due to the constraint of discarding pairs of rods that may affect each other, $\rho_\Omega^E(r)$ is only calculated at relatively large separation, which limits access to the small-scale correlation levels. Its trend, however, is consistent with a characteristic scale of the surface vorticity field around $10\eta$. This is somewhat larger than but comparable to the size of intense vortex cores in 3D turbulence [68–70], as opposed to 2D turbulence where the vorticity field has a correlation length of the order of the forcing scale [71].

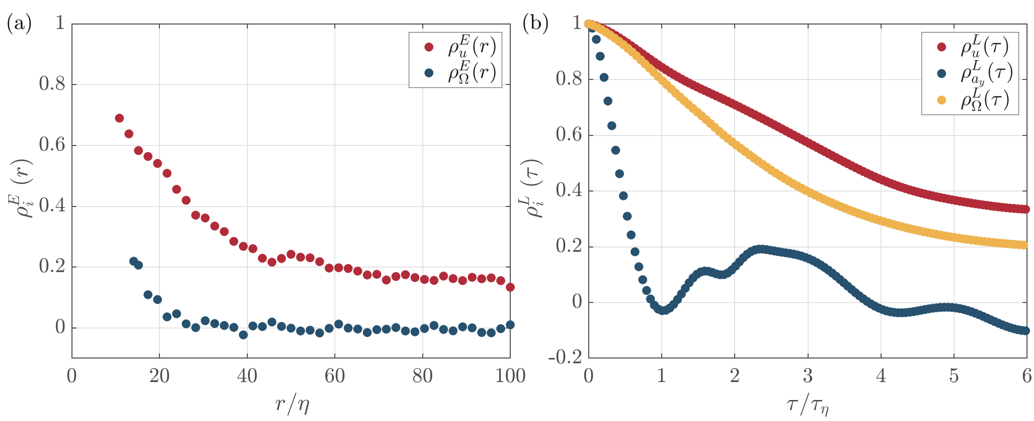


FIG. 5. (a) Eulerian and (b) Lagrangian autocorrelations of spheres' linear motion and rods' rotation rates.

The time scales of the surface motion are investigated in the Lagrangian framework. Figure 5(b) displays the temporal autocorrelations of the spheres' velocity and acceleration, as well as the rods' rotation rate: $\rho_u^L(\tau)$, $\rho_a^L(\tau)$, and $\rho_\Omega^L(\tau)$, respectively. As the mean velocity is much larger than the fluctuations, the trajectory length is consistently comparable to the streamwise extent of the FOV. Therefore, the statistics are not significantly biased by the varying trajectory length [72,73]. To estimate the Lagrangian integral time scale $T_L$, we least-square-fit the data to the model of Sawford [74] for the velocity autocorrelation:

$$\rho_u(\tau) = \frac{T_L e^{-\tau/T_L} - T_2 e^{-\tau/T_2}}{T_L - T_2}, \tag{3}$$

where $T_2$ is a time scale related to the finite acceleration variance. The fit returns $T_L = 1.11$ s and $T_2 = 0.03$ s, which are comparable to the bulk values of the Eulerian integral time scale $L/u_{\mathrm{rms}}$ and Kolmogorov time scale $\tau_\eta$, respectively.

By comparison, the autocorrelation of the lateral component of the acceleration $\rho_{a,y}(\tau)$ decays over a much shorter time scale (the streamwise component displaying analogous behavior). In 3D turbulence, individual components of tracer acceleration are known to decay over a time scale $\sim\tau_\eta$: Numerical simulations by Yeung and Pope [75] found zero-crossing at $\sim 2\tau_\eta$, while experiments by Voth *et al*. [51] found e-fold decorrelation at $\sim 0.7\tau_\eta$. We observe a similar trend for the present free-surface turbulence. The oscillations of $\rho_{a,y}$ at long times are due to limited convergence of this high-order quantity.

In contrast, $\rho_\Omega(\tau)$ decays over a time scale comparable to that of the velocity fluctuations $T_L$. This is at odds with the behavior of 3D turbulence, where the vorticity's characteristic time scale is $\mathcal{O}(\tau_\eta)$ [73,76], and appears closer to the dynamics of 2D turbulence where vortices are long lived [24,77]. This has far-reaching implications for the transport along the surface, as shown in the following.

### C. Particle clustering along the free surface

One aspect that essentially distinguishes the motion of floating particles from tracers in incompressible fluid turbulence is the tendency to cluster. The topology and evolution of this process were investigated from a dynamical system perspective, e.g., by Sommerer and Ott [78], Boffetta *et al.* [29], and Lovecchio, Zonta, and Soldati [20], considering the stretching, contraction, and fractal dimension of the floating tracer fields. This type of analysis requires small-scale information and spatial gradients, not accessible here as we restrict ourselves to a dilute concentration of finite-size particles. Rather, we quantify the spatiotemporal scales of clustering with tools borrowed from studies on inertial particles in turbulence [79,80]. Inertial particles depart from the local fluid pathlines due to their inability to follow its fast fluctuations while floating particles are confined to the surface. Both types of objects describe a compressible field; thus, the approaches devised to characterize a clustering of inertial particles in turbulence are naturally suited for our purposes.

We first consider the radial distribution function (RDF), which describes the scale-by-scale concentration in the surrounding of a generic particle, compared to a uniform distribution [81]. For two-dimensional fields such as those obtained by planar imaging, this is defined as

$$g(r) = (N_r/A_r)/(N_{\mathrm{tot}}/A_{\mathrm{tot}}), \tag{4}$$

where $N_r$ is the number of particles within an annulus of radius $r$ and area $A_r$, and $N_{\mathrm{tot}}$ is the total number of particles within the planar domain of area $A_{\mathrm{tot}}$. In the presence of clustering, the RDF increases for decreasing separations $r$, and the range over which it remains significantly greater than unity indicates the length scale over which clustering occurs [81–83]. The RDF for the floating particles at $\mathrm{Re}_M = 24\,000$, plotted in Fig. 6(a), indicates clustering over length scales $\mathcal{O}(100\eta)$, comparable to the integral scale $L$. When plotted in logarithmic axes, Fig. 6(b), the data appears compatible with a power-law decay which would imply self-similarity of the concentration field. This would be consistent with previous studies that found floaters in free-surface turbulence to

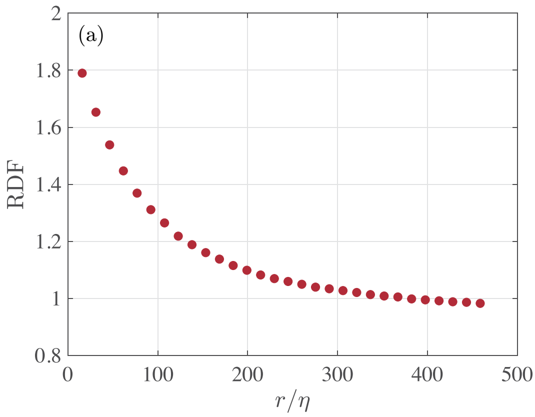


FIG. 6. (a) RDF of the particle distribution on the free surface at $Re_M = 24\,000$. (b) The same data plotted in logarithmic axes.

organize in fractal sets [84,85]. The limited spatial resolution and scaling range, however, do not allow for conclusive statements in this sense.

Particle clustering can also be described by the Voronoï tessellation method: The domain is divided into non-overlapping cells associated to individual particles, each containing a set of points closer to that particle than to any other [86]. Figure 7(a) shows the PDF of the Voronoï cell areas $A_V$ and compares it to the $\Gamma$ function expected for particles distributed in a random Poisson process [87]. The degree of clustering can be quantified by comparing the standard deviation of $A_V$, $\sigma_{A_V}$, against that of a random Poisson process, $\sigma_{\mathrm{RPP}} \sim 0.53$. Here, we find $\sigma_{A_V}/\sigma_{\mathrm{RPP}} \sim 2$, indicating high probability of finding regions of high and low concentrations, i.e., clusters and voids, respectively [86]. For comparison, 2D imaging of inertial particles having Stokes numbers close to unity, which cluster most intensely in turbulence, yields $\sigma_{A_V}/\sigma_{\mathrm{RPP}} \sim 1.5 - 2.5$ [50,88–91].

Finally, we analyze the time scale of clustering by considering the Lagrangian autocorrelation of the particle concentration $c$. The latter is defined for each particle by the inverse of the Voronoi cell area, $c = 1/A_V$, and its characteristic time scale indicates the typical cluster lifetime [92]. Figure 7(b) shows the autocorrelation $\rho_c^L(\tau)$, which decays exponentially with time scale ∼1.1 s,

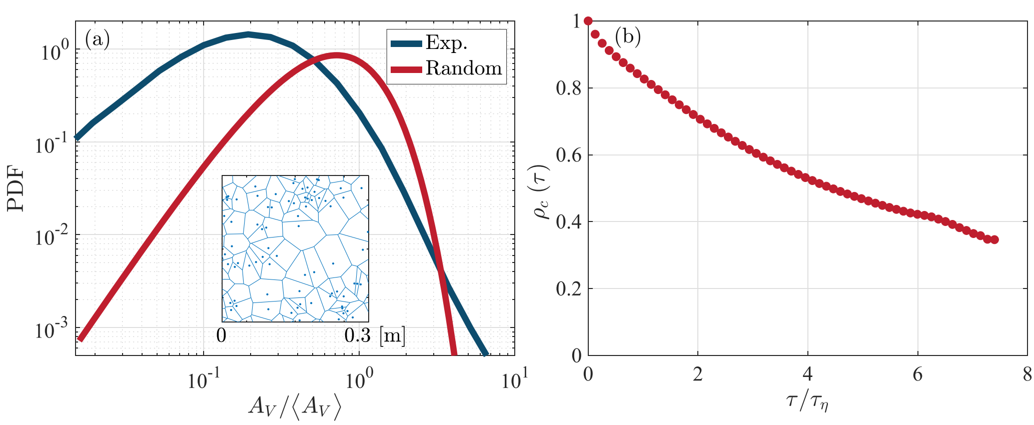


FIG. 7. (a) PDF of the areas of the Voronoï cells around particles along the free surface at $\mathrm{Re}_M = 24\,000$ (example cells shown in the inset), compared to the PDF obtained for a random Poisson process. (b) Lagrangian autocorrelation of the concentration $c$ based on the Voronoï tessellation, based on the same data.

comparable to the integral time scale $T_L$. By comparison, inertial particles in turbulence form short-lived clusters with a characteristic lifetime $\mathcal{O}(\tau_\eta)$ [92,93].

## IV. DISCUSSION AND CONCLUSIONS

We have studied experimentally the motion and spatial distribution of particles floating along the quasi-flat surface above homogeneous decaying turbulence. This case differs from the majority of previous studies in which the turbulence was generated far from the surface, either by stirring at depth or by mean shear at the bottom wall. In such cases, the turbulence decays toward the surface, and its surface-normal transport is superposed to the effect of the free-surface boundary condition [8]. In the present study, the turbulence is forced by the grid over the entire fluid volume and decays in the surface-parallel direction. Therefore, this case is similar to that of temporally decaying homogeneous turbulence adjacent to a suddenly inserted free surface [9,13,17], at the late stages of its temporal evolution. We have combined PIV along surface-normal and surface-parallel planes with PTV of floating particles that follow the surface fluid. The analysis is based on data obtained in two experimental setups which differ in scale and therefore in Reynolds number. A significantly larger $\mathrm{Re}_M$ compared to our larger-scale setup would imply significant surface deformation (unless the surface tension is enhanced compared to water), while a much smaller $\mathrm{Re}_M$ compared to our smaller-scale case would not match the definition of fully developed turbulence. Therefore, the fact that both setups display the same behavior supports the generality of the conclusions, at least in the case of spatially decaying turbulence. The dynamics of qualitatively different systems, such as wavy surfaces or shear-driven turbulence, are likely to display specific features. Both display the same behavior, which supports the generality of the conclusions.

Let us now come back to the research questions that motivated the study. The first one is: How does the turbulence underneath imprint its features on the surface? The single-point statistics of velocity fluctuations, accelerations, and rotation rates indicate a behavior of the surface similar to the homogeneous turbulence underneath, with comparable levels of TKE, dissipation, acceleration, and vorticity. Therefore, the surface flow scales (from integral to dissipative) reflect those of the turbulence in the bulk. Moreover, the intermittency of the small-scale quantities, in particular the Lagrangian acceleration of small floating particles, agrees with the phenomenology of 3D turbulence rather than 2D turbulence. Analyzing the spatial and temporal scales, however, reveals a more complex picture. Specifically, the surface-attached vortices exhibit long lifetimes comparable to the energetic scales, reminiscent of 2D turbulence.

Long-lived surface vortices were observed already in open channel flows and linked to the quasi-2D nature of the near-surface turbulence (e.g., Kumar, Gupta, and Banerjee [22] and Lovecchio, Zonta, and Soldati [20]). In their mean-shear free-surface flow study, [18] showed that surface-attached vortices decay at a rate comparable to the laminar diffusion of a Lamb vortex, much slower than the expectation from eddy viscosity arguments. They argued, however, that vortex stretching (an inherently 3D process) plays a crucial role in the dynamics which therefore should not be regarded as quasi-2D (see also Walker, Leighton, and Garza-Rios [13]). Ruth and Coletti [16] recently showed how the proximity of the surface hinders the direct cascade of the horizontal component of TKE and causes an inverse cascade of its vertical component, demonstrating how such dynamics are associated with the imbalance between upwellings/downwellings. In the present study, we do not gather sufficiently abundant and spatially resolved data to extract interscale energy fluxes, needed to address the issue of the direction of the energy cascade. We emphasize, however, that this would require full 3D reconstructions of the flow since the spatial nonhomogeneity and the consequent spatial transport of TKE is tightly connected to the interscale energy transfer [94,95].

As found in previous numerical studies [29], we observe that the compressibility ratio grows approaching the surface to approximate the value of 0.5, implying that the surface velocity divergence attains relatively large values with respect to the strain rate and rotation. Indeed, the surface compressibility plays a major role in the surface transport. Using two-point statistics and Helmholtz decomposition of the surface velocity above homogeneous turbulence in a zero-mean flow tank, we recently showed how the divergent component of the velocity field drives anomalously large relative velocities at small scales [36].

Let us turn to the second research question: How do the spatial and temporal scales of free-surface flow shape the scales of the clustering of floating particles? As expected, the compressible nature of the surface flow leads to strong inhomogeneities of the floating particles' distribution. Here, we have used RDFs and Voronoi tessellation to characterize the intensity of particle clustering and its spatiotemporal scales. Remarkably, clustering extends up to the integral scales of the flow both in spatial extent and in temporal duration. This observation implies that the energetic subsurface eddies directly impact the surface, imprinting their scales on the clusters and voids of the concentration field. More specifically, we hypothesize that the long-lived surface-attached vortices act as attractors for the floating particles. This may be because clusters are correlated with regions of surface divergence [96], which in turn tend to be collocated with surface-attached vortices, as recently demonstrated by Babiker *et al*. [97]. Alternatively, the vortex cores may attract floating particles which are slightly lighter than the fluid. In either case, particles stick to the persistent vortices. These are swept by the energy-containing eddies [43], leading to the observed large-scale modulation of the concentration field in both space and time. The analysis by Chen, Goto, and Vassilicos [98] of inertial clustering in 2D turbulence follows similar lines: In their view, multi-scale clusters are caused by the particles sticking to zero-acceleration points swept by the energetic eddies. In order to verify this picture (and the analogy with inertial particles), detailed measurements of the small-scale features of the surface velocity field are needed, and efforts in this direction are underway.

We remark that the long-lifetime vortices may entrap particles within a specific range of scales, resulting in a temporary slowdown of particle dispersion. Investigating this phenomenon necessitates high-resolution measurements of the velocity field coupled with precise particle tracking techniques. Although such an analysis extends beyond the scope of the present study, it represents a valuable direction for future research. A more detailed exploration of these effects would significantly enhance our understanding of the intricate interplay between vortex dynamics and particle dispersion.

In the present configuration, there is effectively no mean shear nor confinement from below the surface. In several previous studies in open channels, on the other hand, the depth was comparable to or smaller than the largest scales of motion (e.g., [22]; [99]). Several experiments in shallow turbulent flows have displayed a superposition of 2D and 3D dynamics, e.g., in grid turbulence [100], meandering jets [101], and electromagnetically driven layers [102]. Numerical simulations in thin domains have also shown that spatial confinement leads to the coexistence of 2D and 3D turbulence phenomenology, using fully periodic boundary conditions [103,104] and recently also in the presence of a free surface [105]. The effect of confinement deserves further scrutiny, as it may lead to conclusions of maximum generality. Finally, we note that our findings on the spatial and temporal scales of the motion of floaters may be relevant to other systems that exhibit effective compressibility and turbulent-like behavior, such as phoretic and self-propelled particles [106–108].

## ACKNOWLEDGMENTS

Funding from the Swiss National Science Foundation (Project No. 207318) is gratefully acknowledged. We gratefully acknowledge the contribution of Nico Metzger in carrying out the PTV measurements of the floating rods.

## APPENDIX A: COMPARISON BETWEEN 1 mm AND 2 mm PARTICLES

The behavior of the two types of floating particles utilized, 1 mm and 2 mm in diameter, is found to be indistinguishable within experimental scatter. This is shown in Fig. 8 for the PDF of velocity fluctuations and accelerations in the streamwise direction.

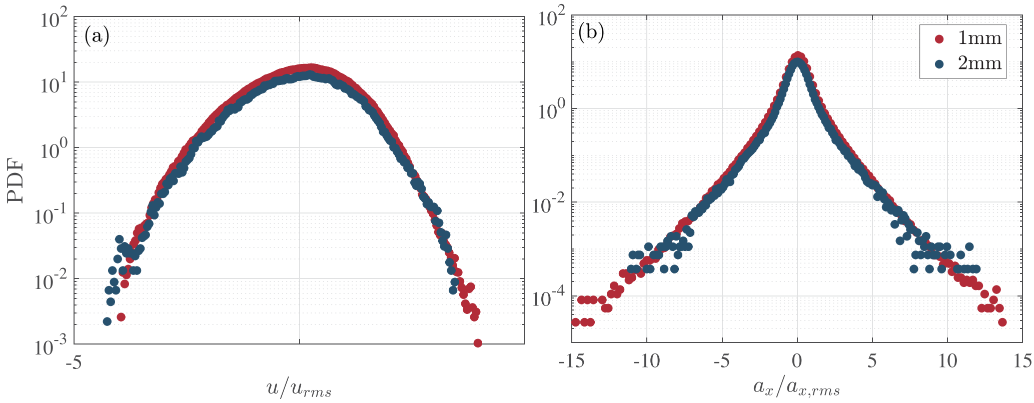


FIG. 8. Comparison between the 1 mm and 2 mm floating particles for (a) streamwise velocity fluctuations and (b) streamwise accelerations measured at $\mathrm{Re}_M = 24\,000$.

### APPENDIX B: COMPARISON BETWEEN $\mathrm{Re}_M = 8350$ and $\mathrm{Re}_M = 24000$

Figure 9 compares the surface flow statistics for the cases $\mathrm{Re}_M = 8350$ and $\mathrm{Re}_M = 24\,000$ for selected quantities, namely the PDFs of velocity fluctuations and acceleration, the Lagrangian

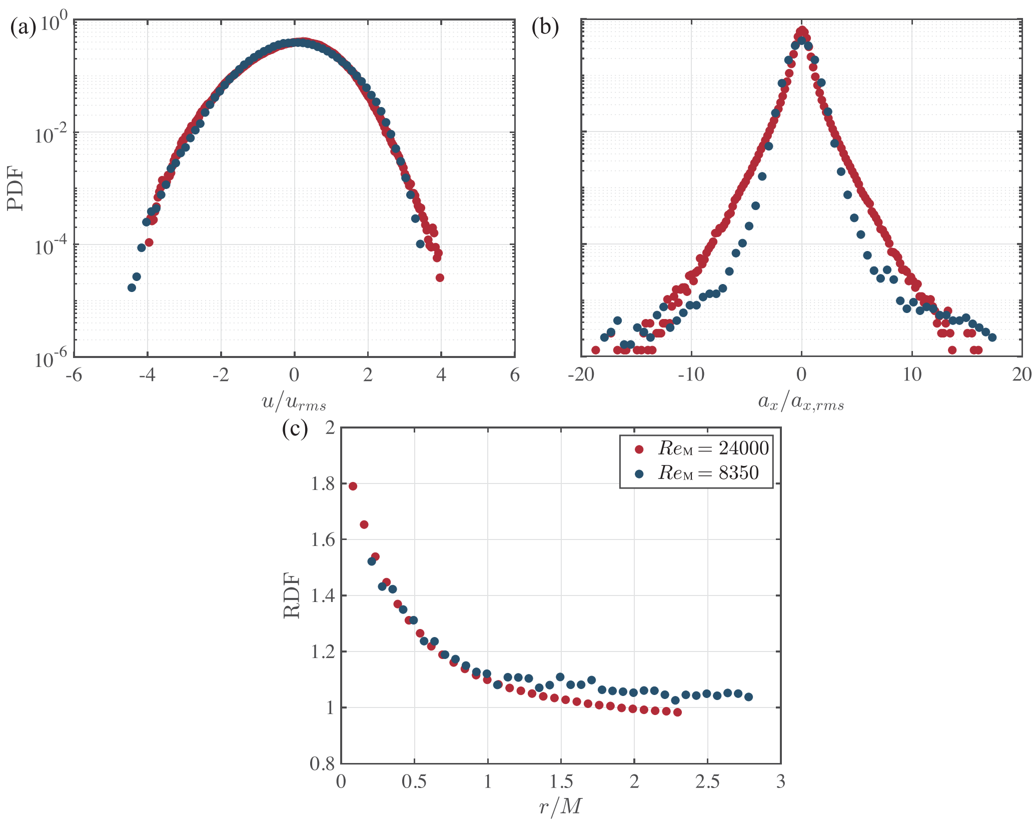


FIG. 9. Selected comparison of the surface flow between the cases at $\mathrm{Re}_M = 8350$ and 24 000, in terms of (a) PDF of velocity streamwise fluctuations, (b) PDF of streamwise acceleration, and (c) RDF of the spherical particles.

autocorrelation of the velocity fluctuations, and the RDF. In the latter, the separation is normalized by the $M$, which highlights how the clustering extends over the integral scales for both considered cases.

---


[1] B. Jähne and H. Haussecker, Air-water gas exchange, Annu. Rev. Fluid Mech. **30**, 443 (1998).

[2] Å. Horgby, P. L. Segatto, E. Bertuzzo, R. Lauerwald, B. Lehner, A. J. Ulseth, T. W. Vennemann, and T. J. Battin, Unexpected large evasion fluxes of carbon dioxide from turbulent streams draining the world's mountains, Nat. Commun. **10**, 4888 (2019).

[3] L. Deike, Mass transfer at the ocean-atmosphere interface: the role of wave breaking, droplets, and bubbles, Annu. Rev. Fluid Mech. **54**, 191 (2022).

[4] E. van Sebille, S. Aliani, K. L. Law, N. Maximenko, J. M. Alsina, A. Bagaev, M. Bergmann, B. Chapron, I. Chubarenko, A. Cózar *et al.*, The physical oceanography of the transport of floating marine debris, Environ. Res. Lett. **15**, 023003 (2020).

[5] T. van Emmerik and A. Schwarz, Plastic debris in rivers, WIREs Water **7**, e1398 (2020).

[6] M. Brocchini and D. H. Peregrine, The dynamics of strong turbulence at free surfaces. Part 1. Description, J. Fluid Mech. **449**, 225 (2001).

[7] B. K. Smeltzer, O. Rømcke, R. J. Hearst, and S. r. Ellingsen, Experimental study of the mutual interactions between waves and tailored turbulence, J. Fluid Mech. **962**, R1 (2023).

[8] J. Magnaudet, High-Reynolds-number turbulence in a shear-free boundary layer: Revisiting the hunt-graham theory, J. Fluid Mech. **484**, 167 (2003).

[9] J. C. R. Hunt and J. M. R. Graham, Free-stream turbulence near plane boundaries, J. Fluid Mech. **84**, 209 (1978).

[10] T. Uzkan and W. C. Reynolds, A shear-free turbulent boundary layer, J. Fluid Mech. **28**, 803 (1967).

[11] N. H. Thomas and P. E. Hancock, Grid turbulence near a moving wall, J. Fluid Mech. **82**, 481 (1977).

[12] B. H. Brumley and G. H. Jirka, On the normalized turbulent energy dissipation rate, J. Fluid Mech. **183**, 235 (1987).

[13] D. T. Walker, R. I. Leighton, and L. O. Garza-Rios, Shear-free turbulence near a flat free surface, J. Fluid Mech. **320**, 19 (1996).

[14] X. Guo and L. Shen, Interaction of a deformable free surface with statistically steady homogeneous turbulence, J. Fluid Mech. **658**, 33 (2010).

[15] E. A. Variano and E. A. Cowen, Turbulent transport of a high-Schmidt-number scalar near an air-water interface, J. Fluid Mech. **731**, 259 (2013).

[16] D. J. Ruth and F. Coletti, Structure and energy transfer in homogeneous turbulence below a free surface, J. Fluid Mech. **1001**, A46 (2024).

[17] B. Perot and P. Moin, Shear-free turbulent boundary layers. Part 1. Physical insights into near-wall turbulence, J. Fluid Mech. **295**, 199 (1995).

[18] L. Shen, X. Zhang, D. K. Yue, and G. S. Triantafyllou, The surface layer for free-surface turbulent flows, J. Fluid Mech. **386**, 167 (1999).

[19] M. A. C. Teixeira and S. E. Belcher, Dissipation of shear-free turbulence near boundaries, J. Fluid Mech. **422**, 167 (2000).

[20] S. Lovecchio, F. Zonta, and A. Soldati, Upscale energy transfer and flow topology in free-surface turbulence, Phys. Rev. E **91**, 033010 (2015).

[21] Y. Pan and S. Banerjee, A numerical study of free-surface turbulence in channel flow, Phys. Fluids **7**, 1649 (1995).

[22] S. Kumar, R. Gupta, and S. Banerjee, An experimental investigation of the characteristics of free-surface turbulence in channel flow, Phys. Fluids **10**, 437 (1998).

[23] N. Nagaosa, *Quantum Field Theory in Condensed Matter Physics* (Springer Science & Business Media, Berlin, 1999).

[24] P. Davidson, *Turbulence. an Introduction for Scientists and Engineers* (Oxford University Press, 2004).
[25] P. L. Johnson, Energy transfer from large to small scales in turbulence by multiscale nonlinear strain and vorticity interactions, Phys. Rev. Lett. **124**, 104501 (2020).
[26] H. Sanness Salmon, L. J. Baker, J. L. Kozarek, and F. Coletti, Effect of shape and size on the transport of floating particles on the free surface in a natural stream, Water Resour. Res. **59**, e2023WR035716 (2023).
[27] G. T. Csanady, Turbulent diffusion in lake huron, J. Fluid Mech. **17**, 360 (1963).
[28] B. Eckhardt and J. Schumacher, Turbulence and passive scalar transport in a free-slip surface, Phys. Rev. E **64**, 016314 (2001).
[29] G. Boffetta, J. Davoudi, B. Eckhardt, and J. Schumacher, Lagrangian tracers on a surface flow: The role of time correlations, Phys. Rev. Lett. **93**, 134501 (2004).
[30] W. I. Goldburg, J. R. Cressman, Z. Vörös, B. Eckhardt, and J. Schumacher, Turbulence in a free surface, Phys. Rev. E **63**, 065303(R) (2001).
[31] J. R. Cressman, J. Davoudi, W. I. Goldburg, and J. Schumacher, Eulerian and Lagrangian studies in surface flow turbulence, New J. Phys. **6**, 53 (2004).
[32] J. R. Cressman and W. I. Goldburg, Compressible flow: Turbulence at the surface, J. Stat. Phys. **113**, 875 (2003).
[33] D. E. Turney and S. Banerjee, Air–water gas transfer and near-surface motions, J. Fluid Mech. **733**, 588 (2013).
[34] S. Protière, Particle rafts and armored droplets, Annu. Rev. Fluid Mech. **55**, 459 (2023).
[35] T. Ishihara, Y. Kaneda, M. Yokokawa, K. I. Itakura, and A. Uno, Small-scale statistics in high-resolution direct numerical simulation of turbulence: Reynolds number dependence of one-point velocity gradient statistics, J. Fluid Mech. **592**, 335 (2007).
[36] Y. Li, Y. Wang, Y. Qi, and F. Coletti, Relative dispersion in free-surface turbulence, J. Fluid Mech. **993**, R2 (2024).
[37] Y. Zhao, Y. Xue, S. Mei, Y. Chao, and J. Carmeliet, Enhancement of heat removal from street canyons due to buoyant approaching flow: Water tunnel PIV-LIF measurements, Build. Environ. **226**, 109757 (2022).
[38] Z. Xu, B. Kaszás, M. Cenedese, G. Berti, F. Coletti, and G. Haller, Data-driven modelling of the regular and chaotic dynamics of an inverted flag from experiments, J. Fluid Mech. **987**, R7 (2024).
[39] R. J. Hearst and P. Lavoie, Decay of turbulence generated by a square-fractal-element grid, J. Fluid Mech. **741**, 567 (2014).
[40] R. J. Hearst, *Fractal, Classical, and Active Grid Turbulence: From Production to Decay* (University of Toronto, Canada, 2015).
[41] B. Ganapathisubramani, K. Lakshminarasimhan, and N. T. Clemens, Determination of complete velocity gradient tensor by using cinematographic stereoscopic piv in a turbulent jet, Exp. Fluids **42**, 923 (2007).
[42] W. K. George and H. J. Hussein, Locally axisymmetric turbulence, J. Fluid Mech. **233**, 1 (1991).
[43] H. Tennekes and J. L. Lumley, *A First Course in Turbulence* (MIT Press, Cambridge, Massachusetts, 1972).
[44] S. B. Pope, *Turbulent Flows* (Cambridge University Press, Cambridge, UK, 2000).
[45] A. N. Kolmogorov, The local structure of turbulence in incompressible viscous fluid for very large Reynolds numbers, Dokl. Akad. Nauk SSSR **30**, 301 (1941).
[46] H. Homann and J. Bec, Finite-size effects in the dynamics of neutrally buoyant particles in turbulent flow, J. Fluid Mech. **651**, 81 (2010).
[47] R. Volk, E. Calzavarini, E. Leveque, and J. F. Pinton, Dynamics of inertial particles in a turbulent von Kármán flow, J. Fluid Mech. **668**, 223 (2011).
[48] T. Berk and F. Coletti, An analytical model for the slip velocity of particles in turbulence, J. Fluid Mech. **996**, A1 (2024).
[49] Z. Zhang, A flexible new technique for camera calibration, IEEE Trans. Pattern Anal. Machine Intell. **22**, 1330 (2000).
[50] A. J. Petersen, L. Baker, and F. Coletti, Experimental study of inertial particles clustering and settling in homogeneous turbulence, J. Fluid Mech. **864**, 925 (2019).

[51] G. A. Voth, A. La Porta, A. M. Crawford, J. Alexander, and E. Bodenschatz, Measurement of particle accelerations in fully developed turbulence, J. Fluid Mech. **469**, 121 (2002).
[52] T. Berk and F. Coletti, Dynamics of small heavy particles in homogeneous turbulence: A Lagrangian experimental study, J. Fluid Mech. **917**, A47 (2021).
[53] L. J. Baker and F. Coletti, Particle–fluid–wall interaction of inertial spherical particles in a turbulent boundary layer, J. Fluid Mech. **908**, A39 (2021).
[54] L. J. Baker and F. Coletti, Experimental investigation of inertial fibres and disks in a turbulent boundary layer, J. Fluid Mech. **943**, A27 (2022).
[55] S. Gerashchenko, N. S. Sharp, S. Neuscamman, and Z. Warhaft, Lagrangian measurements of inertial particle accelerations in a turbulent boundary layer, J. Fluid Mech. **617**, 255 (2008).
[56] M. Ebrahimian, R. S. Sanders, and S. Ghaemi, Dynamics and wall collision of inertial particles in a solid-liquid turbulent channel flow, J. Fluid Mech. **881**, 872 (2019).
[57] S. Parsa, J. S. Guasto, M. Kishore, N. T. Ouellette, J. P. Gollub, and G. A. Voth, Rotation and alignment of rods in two-dimensional chaotic flow, Phys. Fluids **23**, 043302 (2011).
[58] S. Parsa, E. Calzavarini, F. Toschi, and G. A. Voth, Rotation rate of rods in turbulent fluid flow, Phys. Rev. Lett. **109**, 134501 (2012).
[59] R. Ni, S. Kramel, N. T. Ouellette, and G. A. Voth, Measurements of the coupling between the tumbling of rods and the velocity gradient tensor in turbulence, J. Fluid Mech. **766**, 202 (2015).
[60] S. Brizzolara, M. E. Rosti, S. Olivieri, L. Brandt, M. Holzner, and A. Mazzino, Fiber tracking velocimetry for two-point statistics of turbulence, Phys. Rev. X **11**, 031060 (2021).
[61] H. Herlina and J. G. Wissink, Direct numerical simulation of turbulent scalar transport across a flat surface, J. Fluid Mech. **744**, 217 (2014).
[62] I. Calmet and J. Magnaudet, Statistical structure of high-Reynolds-number turbulence close to the free surface of an open-channel flow, J. Fluid Mech. **474**, 355 (2003).
[63] G. Boffetta and R. E. Ecke, Two-dimensional turbulence, Annu. Rev. Fluid Mech. **44**, 427 (2012).
[64] P. Lavoie, L. Djenidi, and R. A. Antonia, Effects of initial conditions in decaying turbulence generated by passive grids, J. Fluid Mech. **585**, 395 (2007).
[65] M. Sinhuber, E. Bodenschatz, and G. P. Bewley, Decay of turbulence at high Reynolds numbers, Phys. Rev. Lett. **114**, 034501 (2015).
[66] A. S. Monin and A. M. Yaglom, *Statistical Fluid Mechanics* (MIT Press, 1975).
[67] B. L. Sawford, P. K. Yeung, M. S. Borgas, P. Vedula, A. La Porta, A. M. Crawford, and E. Bodenschatz, Conditional and unconditional acceleration statistics in turbulence, Phys. Fluids **15**, 3478 (2003).
[68] J. Jiménez, A. A. Wray, P. G. Saffman, and R. S. Rogallo, The structure of intense vorticity in isotropic turbulence, J. Fluid Mech. **255**, 65 (1993).
[69] T. Ishihara, Y. Kaneda, and J. C. R. Hunt, Thin shear layers in high Reynolds number turbulence—DNS results, Flow, Turbul. Combust. **91**, 895 (2013).
[70] D. W. Carter and F. Coletti, Small-scale structure and energy transfer in homogeneous turbulence, J. Fluid Mech. **854**, 505 (2018).
[71] A. J. Lowe and P. A. Davidson, The evolution of freely-decaying, isotropic, two-dimensional turbulence, Eur. J. Mech. B Fluids **24**, 314 (2005).
[72] N. Mordant, A. M. Crawford, and E. Bodenschatz, Experimental Lagrangian acceleration probability density function measurement, Physica D **193**, 245 (2004).
[73] M. Guala, A. Liberzon, A. Tsinober, and W. Kinzelbach, An experimental investigation on Lagrangian correlations of small-scale turbulence at low Reynolds number, J. Fluid Mech. **574**, 405 (2007).
[74] B. L. Sawford, Reynolds number effects in Lagrangian stochastic models of turbulent dispersion, Phys. Fluids A **3**, 1577 (1991).
[75] P. K. Yeung and S. B. Pope, Lagrangian statistics from direct numerical simulations of isotropic turbulence, J. Fluid Mech. **207**, 531 (1989).
[76] P. K. Yeung, Lagrangian investigations of turbulence, Annu. Rev. Fluid Mech. **34**, 115 (2002).
[77] M. K. Rivera and R. E. Ecke, Lagrangian statistics in weakly forced two-dimensional turbulence, Chaos **26**, 013103 (2016).

[78] J. C. Sommerer and E. Ott, Particles floating on a moving fluid: A dynamically comprehensible physical fractal, Science **259**, 335 (1993).
[79] S. Balachandar and J. K. Eaton, Turbulent dispersed multiphase flow, Annu. Rev. Fluid Mech. **42**, 111 (2010).
[80] L. Brandt and F. Coletti, Particle-laden turbulence: Progress and perspectives, Annu. Rev. Fluid Mech. **54**, 159 (2022).
[81] S. Sundaram and L. R. Collins, Collision statistics in an isotropic particle-laden turbulent suspension. Part 1. Direct numerical simulations, J. Fluid Mech. **335**, 75 (1997).
[82] A. M. Wood, W. Hwang, and J. K. Eaton, Preferential concentration of particles in homogeneous and isotropic turbulence, Int. J. Multiphase Flow **31**, 1220 (2005).
[83] P. J. Ireland, A. D. Bragg, and L. R. Collins, The effect of Reynolds number on inertial particle dynamics in isotropic turbulence. Part 1. Simulations without gravitational effects, J. Fluid Mech. **796**, 617 (2016).
[84] G. Boffetta, J. Davoudi, and F. D. Lillo, Multifractal clustering of passive tracers on a surface flow, Europhys. Lett. **74**, 62 (2006).
[85] J. Larkin, M. M. Bandi, A. Pumir, and W. I. Goldburg, Power-law distributions of particle concentration in free-surface flows, Phys. Rev. E **80**, 066301 (2009).
[86] R. Monchaux, M. Bourgoin, and A. Cartellier, Preferential concentration of heavy particles: A Voronoï analysis, Phys. Fluids **22**, 103304 (2010).
[87] J. S. Ferenc and Z. Néda, On the size distribution of poisson Voronoi cells, Physica A **385**, 518 (2007).
[88] R. Monchaux, M. Bourgoin, and A. Cartellier, Analyzing preferential concentration and clustering of inertial particles in turbulence, Int. J. Multiphase Flow **40**, 1 (2012).
[89] S. Sumbekova, A. Cartellier, A. Aliseda, and M. Bourgoin, Preferential concentration of inertial sub-Kolmogorov particles: The roles of mass loading of particles, stokes numbers, and Reynolds numbers, Phys. Rev. Fluids **2**, 024302 (2017).
[90] L. J. Baker, A. Frankel, A. Mani, and F. Coletti, Coherent clusters of inertial particles in homogeneous turbulence, J. Fluid Mech. **833**, 364 (2017).
[91] R. Hassaini, A. J. Petersen, and F. Coletti, Effect of two-way coupling on clustering and settling of heavy particles in homogeneous turbulence, J. Fluid Mech. **976**, A12 (2023).
[92] Y. Tagawa, J. M. Mercado, V. N. Prakash, E. Calzavarini, C. Sun, and D. Lohse, Three-dimensional Lagrangian Voronoï analysis for clustering of particles and bubbles in turbulence, J. Fluid Mech. **693**, 201 (2012).
[93] Y. Liu, L. Shen, R. Zamansky, and F. Coletti, Life and death of inertial particle clusters in turbulence, J. Fluid Mech. **902**, R1 (2020).
[94] A. Chiarini, D. Gatti, A. Cimarelli, and M. Quadrio, Structure of turbulence in the flow around a rectangular cylinder, J. Fluid Mech. **946**, A35 (2022).
[95] A. Cimarelli, G. Boga, A. Pavan, P. Costa, and E. Stalio, Spatially evolving cascades in wall turbulence with and without interface, J. Fluid Mech. **987**, A4 (2024).
[96] S. Lovecchio, C. Marchioli, and A. Soldati, Time persistence of floating-particle clusters in free-surface turbulence, Phys. Rev. E **88**, 033003 (2013).
[97] O. M. Babiker, I. Bjerkebæk, A. Xuan, L. Shen, and S. Å. Ellingsen, Vortex imprints on a free surface as proxy for surface divergence, J. Fluid Mech. **964**, R2 (2023).
[98] L. Chen, S. Goto, and J. C. Vassilicos, Turbulent clustering of stagnation points and inertial particles, J. Fluid Mech. **553**, 143 (2006).
[99] V. Nikora, R. Nokes, W. Veale, M. Davidson, and G. H. Jirka, Large-scale turbulent structure of uniform shallow free-surface flows, Environ. Fluid Mech. **7**, 159 (2007).
[100] W. S. J. Uijttewaal and G. H. Jirka, Grid turbulence in shallow flows, J. Fluid Mech. **489**, 325 (2003).
[101] M. Miozzi, F. Lalli, and G. P. Romano, Experimental investigation of a free-surface turbulent jet with Coanda effect, Exp. Fluids **49**, 341 (2010).
[102] H. Xia, D. Byrne, G. Falkovich, and M. Shats, Upscale energy transfer in thick turbulent fluid layers, Nat. Phys. **7**, 321 (2011).
[103] A. Celani, S. Musacchio, and D. Vincenzi, Turbulence in more than two and less than three dimensions, Phys. Rev. Lett. **104**, 184506 (2010).

[104] S. Musacchio and G. Boffetta, Split energy cascade in turbulent thin fluid layers, Phys. Fluids **29**, 111106 (2017).
[105] G. Boffetta, S. Musacchio, A. Mazzino, and M. E. Rosti, Transient inverse energy cascade in free surface turbulence, Phys. Rev. Fluids **8**, 034601 (2023).
[106] V. Shukla, R. Volk, M. Bourgoin, and A. Pumir, Phoresis in turbulent flows, New J. Phys. **19**, 123030 (2017).
[107] M. Bourgoin, R. Kervil, C. Cottin-Bizonne, F. Raynal, R. Volk, and C. Ybert, Kolmogorovian active turbulence of a sparse assembly of interacting marangoni surfers, Phys. Rev. X **10**, 021065 (2020).
[108] C. Gouiller, F. Raynal, L. Maquet, M. Bourgoin, C. Cottin-Bizonne, R. Volk, and C. Ybert, Mixing and unmixing induced by active camphor particles, Phys. Rev. Fluids **6**, 014501 (2021).